THE JOURNAL OF PHYSICAL CHEMISTRY C

ARTICLE

pubs.acs.org/JPCC

Structural Evolution of Plasma-Sputtered Core−Shell Nanoparticles for Catalytic Combustion of Methane

Xiaoning Guo,[†,§] Pascal Brault,[*,‡] Guojuan Zhi,[†,§] Amaël Caillard,[‡] Guoqiang Jin,[†] and Xiangyun Guo[*,†]

[†]State Key Laboratory of Coal Conversion, Institute of Coal Chemistry, Taiyuan 030001, People's Republic of China

[‡]GREMI UMR6606 CNRS - Université d'Orléans BP6744, 45067 Orleans Cedex2, France

[§]Graduate University of the Chinese Academy of Sciences, Beijing 100039, People's Republic of China

ABSTRACT: Fe@Pd, Fe@Pt, and Fe@Au core−shell nanoparticles supported by silicon carbide have been prepared by plasma sputtering deposition and employed as the catalyst for methane combustion. The core−shell catalysts exhibit higher activities than single metallic catalysts due to surface alloying effects. With the surface alloying of the core−shell nanoparticles, Pd−O and Pt−O bonds become weak because the increase of the electron cloud density around Pd and Pt atoms due to the electron transfer from surface Fe to Pd or Pt atoms. Therefore, the activities of Fe@Pd/SiC and Fe@Pt/SiC increase with the reaction time. The activity of Fe@Au/SiC keeps invariant in the reaction because the Fe@Au core−shell structure has high stability. Transmission electron microscopy and X-ray photoelectron spectroscopy results further confirm the structural evolution.

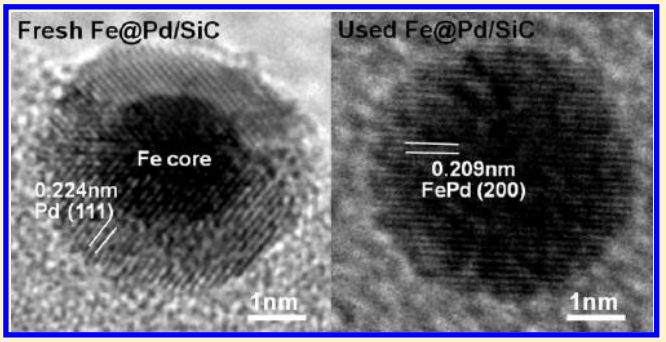

1. INTRODUCTION

Core−shell bimetallic nanoparticles have been extensively studied and widely applied in heterogeneous catalysis, such as CO oxidation, the oxygen reduction reaction, and ethanol oxidation.[1−7] Usually, the shell layers of core−shell nanoparticles are noble metals; therefore, the core−shell structures are ideal architectures for reducing the dosage of noble metals and improving the activity of catalysts. However, very few studies are devoted to investigating the stability of the core−shell structured nanoparticles in catalytic reactions especially under high temperatures.[8] Moreover, it is argued that catalytic core−shell nanoparticles are certainly superior to other structures, such as alloys. For example, Mizukoshi et al. claimed that a Au/Pd random alloy supported on TiO_2 exhibited higher activity than TiO_2-supported Au@Pd core−shell nanoparticles in photochemical evolution of H_2 from ethanol aqueous solutions under UV illumination.[9]

Various preparation techniques, such as sequential synthesis and arc discharge, have been proposed for preparation of core−shell structured catalysts.[10−13] Recently, plasma sputtering deposition has been studied extensively because the technique is feasible and no post-treatment is needed.[14,15] Considerable studies are devoted to preparation of bimetallic nanoparticles, suggesting that the plasma sputtering deposition has obvious advantages in controlling the composition of bimetallic nanoparticles.[16−18]

Catalytic combustion of a lean natural gas and air mixture has attracted considerable attention because the process operates at low temperature and produces little NO_x emission.[19−21] Supported noble metals (Pd, Pt, and Au) have been found to have high catalytic activities for the methane combustion.[19,20,22] However, noble metals are very rare and expensive. Because the activities of different catalysts are mainly related to the surface composition of metallic particles, localizing noble metals as a thin shell on common metal cores is expected to not only reduce the dosage of noble metals but also enhance the catalytic activity.

In this work, we have prepared silicon carbide-supported Fe@Pd, Fe@Pt, and Fe@Au core−shell bimetallic nanoparticles using the plasma sputtering deposition method and investigated the compositional and structural evolution of the different core−shell nanoparticles by transmission electron microscopy and X-ray photoelectron spectroscopy. The variation in the catalytic performance of the core−shell bimetallic catalysts reveals the structural evolution of core−shell nanoparticles in the reaction.

2. EXPERIMENTS

2.1. Catalyst Preparation. Fe, Pd, Pt, and Au sputtering depositions were performed in a cylindrical stainless steel low-pressure transformer coupled plasma device. The experimental setup dedicated to the study has been described elsewhere.[23,24] Briefly, argon plasma was created in a chamber using a planar external rf antenna (13.56 MHz, 300 W). The substrate used in this work is high-surface-area SiC,[25,26] which is prepared from a sol−gel and carbothermal reduction route and has a specific surface area of 50.8 $m^2\ g^{-1}$ and a pore volume of 0.13 $cm^3\ g^{-1}$.

Received: July 12, 2011
Revised: September 29, 2011
Published: October 25, 2011

Table 1. Loadings of Different Metals, the Average Size of Nanoparticles, and the Shell Thickness of Fe@Pd/SiC, Fe@Pt/SiC, and Fe@Au/SiC

	metal loading (ICP-MS) (wt %)											
	Fe		Pd		Pt		Au		nanoparticle size (TEM) (nm)		shell thickness (nm)	
sample	fresh	used	fresh	used	fresh	used	fresh	used	fresh	used	fresh	used
Fe@Pd/SiC	0.18	0.17	0.31	0.30					4.2	4.5	1.1	
Fe@Pt/SiC	0.16	0.16			0.33	0.31			3.4	3.6	0.9	
Fe@Au/SiC	0.18	0.17					0.33	0.33	4.5	4.8	1.2	1.3

The plasma depositions were performed under P = 0.5 Pa and V_b = −200 V, where P is the Ar pressure (the base pressure is 5×10^{-5} Pa) and V_b is the bias voltage of metal targets. All the targets are analytically pure (99.99 wt %) single metals. The side length of Fe and Pt square targets is 25 mm, and the diameter of Pd and Au circular targets is 25 mm. For preparing core−shell structured nanoparticles, the deposition time was first set up as 20 min for Fe deposition and then 7.5, 7.5, and 3.75 min for Pd, Pt, and Au deposition, respectively. The corresponding samples are marked as Fe@Pd/SiC, Fe@Pt/SiC, and Fe@Au/SiC. For comparison, single metallic catalysts were also prepared. The deposition time for Fe, Pd, Pt, and Au is 50, 12.5, 12.5, and 6.25 min, respectively. The corresponding samples are marked as Fe/SiC, Pd/SiC, Pt/SiC, and Au/SiC.

2.2. Catalytic Test. The catalytic performance of different catalysts for methane combustion was carried out in a fixed-bed quartz reactor with an inner diameter of 8 mm at atmospheric pressure, and the mixture of O_2(20%)/CH_4(2%)/N_2(78%) was used as the feedstock. A 100 mg portion of the catalyst was packed between two layers of quartz wool. The hourly space velocity was controlled to be 25 000 h^{-1}. Because the deactivation of the SiC-supported catalysts usually demands a long time, a repeated heating-then-cooling cycle method was employed to estimate the stability of different catalysts.[18,27,28] In this method, the catalyst was programmed heated to a temperature at which the reaction achieved a methane conversion of ∼100% at a rate of 5 °C/min. In the heating process, the methane conversion was measured at different temperatures. Afterward, the reactor was cooled to the temperature at which the catalyst just became inactive. The next reaction cycle then began again. Usually, one cycle needs 4 h to finish. The composition of effluent gases was analyzed by a GC-14B gas chromatograph with a TDX-01 column (for separation of H_2, CO, CO_2, O_2, and CH_4) and a TCD detector.

2.3. Catalyst Characterization. The loadings of different metals in the catalysts were determined by a PerkinElmer ELAN 5000 inductively coupled plasma-mass spectroscopy (ICP-MS) instrument. The microstructures of the catalysts were analyzed by using a JEM-2010 high-resolution transmission electron microscope (HRTEM). X-ray photoelectron spectroscopy (XPS) spectra of the catalysts used at different temperatures were measured on an ESCALAB 3 MKII de VG spectrometer by using a Mg Kα (15 kV, 20 mA) X-ray source.

3. RESULTS AND DISCUSSION

3.1. Catalytic Performances. The metal loadings of different core−shell catalysts measured by ICP-MS are listed in Table 1. In the core−shell catalysts, the Fe loadings are around 0.18 wt %

Table 2. Loadings of Different Metals of Fe/SiC, Pd/SiC, Pt/SiC, and Au/SiC

	metal loading (ICP-MS) (wt %)							
	Fe		Pd		Pt		Au	
sample	fresh	used	fresh	used	fresh	used	fresh	used
Fe/SiC	0.52	0.51						
Pd/SiC			0.49	0.48				
Pt/SiC					0.50	0.47		
Au/SiC							0.49	0.49

and the noble metal loadings are around 0.33 wt %. The metal loadings of pure-metal catalysts were also determined by ICP-MS and are around 0.5 wt % (Table 2). From Tables 1 and 2, the loadings of Pd, Pt, and Fe in different catalysts have slight decreases after reaction because of the volatilization of the corresponding metal oxide.

Figure 1 shows the catalytic performances of methane combustion on Fe/SiC, Pd/SiC, and Fe@Pd/SiC. From Figure 1a, Fe/SiC is active only above 650 °C; the methane conversion could reach to 100% at a temperature as high as 780 °C. The activity of Pd/SiC is far better than that of Fe/SiC. The methane conversion on Pd/SiC increases with the reaction temperature in a relatively low temperature. The methane conversion on Pd/SiC begins to decline when the temperature is higher than 550 °C, mainly due to decomposition of the active phase PdO into Pd.[29,30] When employing Fe@Pd/SiC as the catalyst, the methane combustion occurs at about 320 °C and the methane conversion can reach up to 100% at 530 °C. Such low loadings of Pd (0.3 wt.%) in the Fe@Pd core−shell catalyst can thus exhibit higher catalytic activity than Pd/SiC (0.5 wt.%), indicating that the core−shell structure has played an important role in the catalytic reaction. It is widely considered that the excellent catalytic performance of core−shell nanoparticles could be attributed to near surface alloy effects.[31] In the present catalyst, subsurface Pd and Pd−Fe interface layers could effectively affect the binding of adsorbates (CH_4 or O_2) to the Fe@Pd nanoparticle surface, and then the changes in binding enthalpies can enhance the activity of the catalyst in the methane catalytic combustion process. The activity of Fe@Pd/SiC begins to decline at 570 °C, which is slightly higher than that of Pd/SiC (550 °C), indicating that the Fe@Pd structure can effectively delay the declination temperature of Pd-based catalysts.

Figure 1b shows the stability of the Fe@Pd/SiC catalyst in the combustion of methane. Fe@Pd/SiC can keep the methane conversion at almost 100% after 10 reaction cycles, indicating that SiC-supported catalysts have excellent stability in methane combustion

dx.doi.org/10.1021/jp206606r |J. Phys. Chem. C 2011, 115, 24164–24171

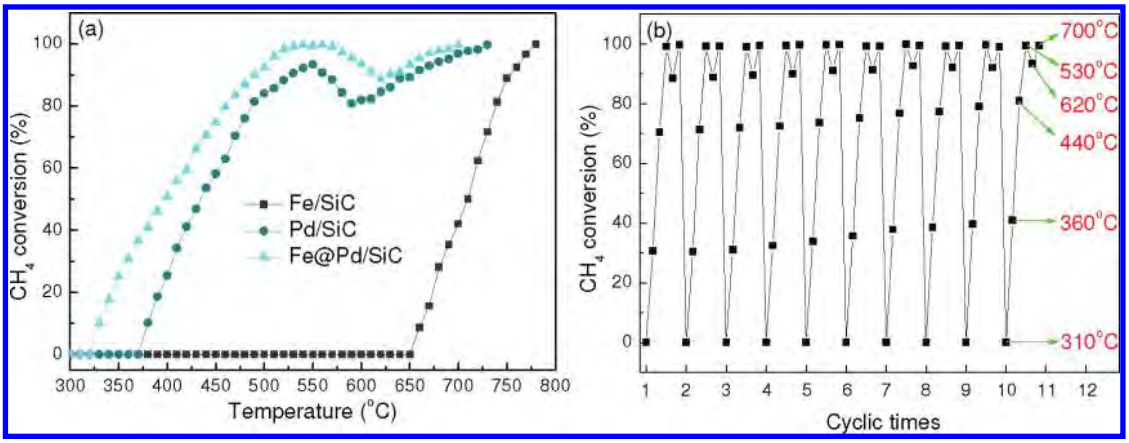

Figure 1. Catalytic activities (a) of Fe/SiC, Pd/SiC, and Fe@Pd/SiC catalysts, and the stability (b) of Fe@Pd/SiC for methane combustion.

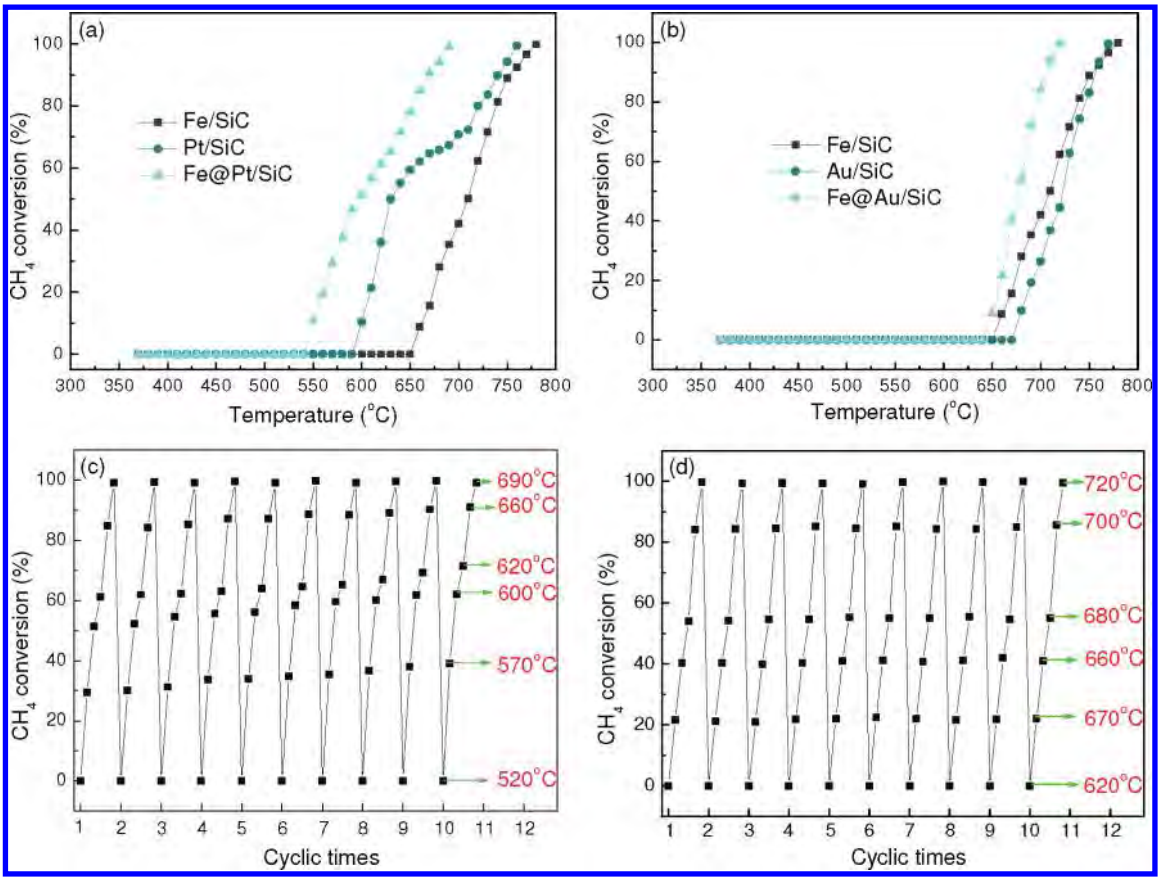

Figure 2. Catalytic activities of Pt/SiC and Fe@Pt/SiC (a) and Au/SiC and Fe@Au/SiC (b) catalysts, and stabilities of Fe@Pt/SiC (c) and Fe@Au/SiC (d) for methane combustion.

due to its high thermal conductivity and good chemical stability.[18,28] The high thermal conductivity is of benefit to the diffusion of reaction heat, which may make active metallic nanoparticles sintered. The good chemical stability can ensure that the support does not react with metallic nanoparticles and produce inactive phases. Meanwhile, the surface of the SiC support we prepared is very rough. It is worth mentioning that the Gibbs−Thomson potential is very large in nanoscale materials with a rough surface. Because of the higher Gibbs−Thomson potential, the interaction between metal particles and the SiC support is higher than that with usual supports. Therefore, the high-surface-area SiC could effectively stabilize the metal nanoparticles. In addition, it can be obviously seen that the methane conversion of Fe@Pd/SiC at low temperatures (lower than the temperature for 100% methane conversion) increases with the cycling times. It is widely known that the activity and selectivity of catalysts extremely depend on their structures.[8] Therefore, the increase in the catalytic activity of Fe@Pd/SiC mainly results from the structural evolution of Fe@Pd core−shell nanoparticles in the catalytic process.

Figure 2 shows the catalytic performances of Pt- and Au-based catalysts for methane combustion. Figure 2a,b indicates that the

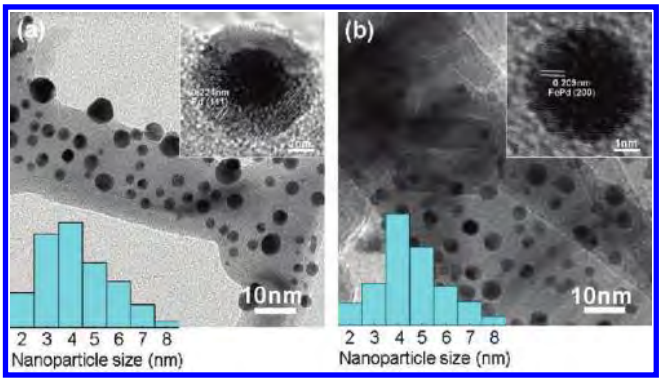

Figure 3. HRTEM images of fresh (a) and used (b) Fe@Pd/SiC catalyst, and the size distribution of nanoparticles.

core−shell catalysts exhibit slightly higher catalytic activity than their corresponding single metallic catalysts. Figure 2c,d shows the stabilities of Fe@Pt/SiC and Fe@Au/SiC catalysts in the catalytic combustion of methane. Both catalysts can reach a 100% methane conversion and remain unchanged after 10 reaction cycles. These indicate that the high-surface-area SiC as catalyst support can effectively stabilize metallic nanoparticles. The activity of Fe@Pt/SiC increases with the cyclic times, suggesting that the Fe@Pt core−shell structure may produce similar changes as Fe@Pd/SiC during the reaction (Figure 2c). However, the activity of Fe@Au/SiC remains almost unaffected, indicating that the Fe@Au structure can be very stable during the reaction (Figure 2d).

3.2. HRTEM Characterization. Figure 3 shows HRTEM images of fresh and used Fe@Pd/SiC catalysts. From Figure 3a, the Fe@Pd core−shell structure can be clearly observed. Isolated Fe@Pd nanoparticles are highly dispersed on the SiC substrate with an average size of about 4.2 nm (Table 1). The lattice spacing of the shell layer metal is around 0.224 nm, which is indexed as the Pd(111) plane. The Fe cores have an average diameter of about 2 nm and are coated with a 1.1 nm thick Pd layer (Table 1). From Figure 3b, the nanoparticles are still uniformly dispersed on the SiC support after reaction. However, the Fe@Pd core−shell structure has obviously changed into an FePd alloy structure. The lattice spacing of 0.222 nm is indexed as the (111) plane of the FePd alloy.[32] For nanoparticles that contain at least two elements, the surface atoms usually tend to a lower Gibbs free energy to keep the stability of the particles.[33] In our sputtering experiment, Fe atoms are first deposited onto the SiC surface to form nanosized Fe cores. Pd atoms are then deposited onto the Fe-deposited SiC substrate and then coat the Fe cores due to a stronger Pd−Fe interaction than that of Pd−SiC.[32] However, the Gibbs free energy of Fe (~241 mJ/m^2) is lower than that of Pd (~272 mJ/m^2).[34] Therefore, Fe atoms can continually move to the surface to lower the surface free energy of Fe@Pd nanoparticles and form the surface FePd alloy during the cyclic reaction.

Figure 4 shows HRTEM images of fresh and used Fe@Pt/SiC and Fe@Au/SiC catalysts. In these figures, the lattice spacings of nanoparticles are around 0.226, 0.223, and 0.234 nm, which correspond to the Pt(111) plane, PtFe(111) plane, and Au(111) plane, respectively.[35] The nanoparticles of different catalysts are still well-dispersed. From Figure 4a,b, it is obvious that the Fe@Pt core−shell structure has changed into the PtFe alloy after reaction because the Gibbs free energy of Fe is lower than

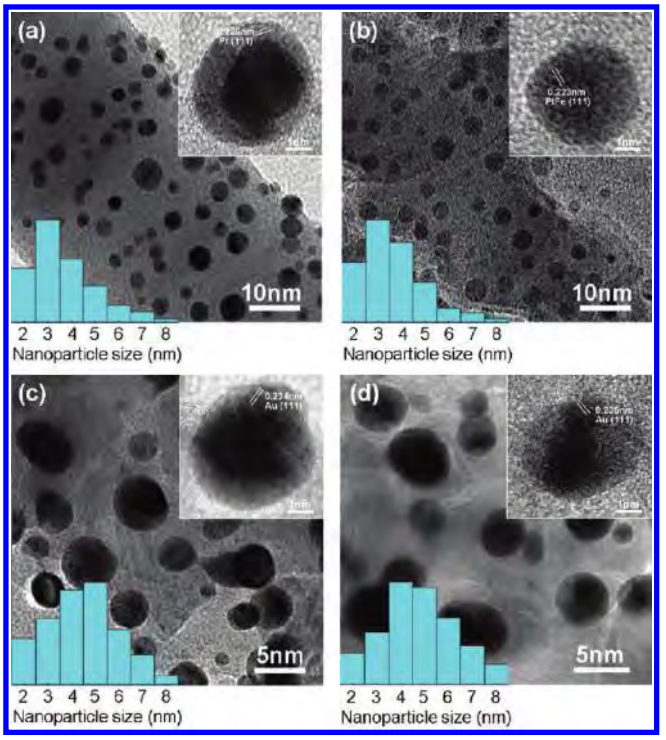

Figure 4. HRTEM images of fresh and used Fe@Pt/SiC (a, b) and Fe@Au/SiC (c, d) catalysts, and the size distribution of nanoparticles.

that of Pt (~299 mJ/m^2).[34] However, the Fe@Au core−shell structure can stably exist even through 10 cyclic reactions, due to the Gibbs free energy of Au (~177 mJ/m^2) being lower than that of Fe.[34] From Table 1 and the HRTEM images, the average sizes of metal nanoparticles in all catalysts only have a slight increase after 10 reaction cycles, indicating that high-surface-area SiC based catalysts have excellent stability.

3.3. XPS Characterization. The XPS spectra of fresh and used Fe@Pd/SiC are shown in Figure 5, and the corresponding binding energies (BEs) of each metal and the derived surface atomic ratios are presented in Table 3. The XPS spectrum of fresh Fe@Pd/SiC shows that the surface atomic ratio (Pd/Fe) of Fe@Pd is 69:31, whereas the surface of Pd nanoparticles in the Pd/SiC is composed of only Pd atoms. Therefore, the fraction of Pd in Pd/SiC exposed in the gas phase available for reaction is larger than that of Fe@Pd/SiC. This further confirms that the higher activity of Fe@Pd/SiC is mainly due to the surface alloy effects. Generally, the BE values of metallic Pd are in the range of 334.7−335.5 eV for Pd $3d_{5/2}$ and 340.3−340.8 eV for Pd $3d_{3/2}$, whereas the BE values of Pd^{2+} are in the range of 337.5−337.8 eV for Pd $3d_{5/2}$ and 342.1−342.6 eV for Pd $3d_{3/2}$.[36−38] From Figure 5a, the Pd BE values of fresh Fe@Pd/SiC are 335.8 and 341.2 eV, which are higher than the BE values of metallic Pd. The higher binding energies are the characteristic of Pd species with a valence between 0 and +2.[39] From Figure 5b, the concentration of Pd^0 is greater than that of Pd^{2+} after reaction. This is due to the decomposition of PdO into Pd. However, the BE values of Pd^0 and Pd^{2+} are lower than those of fresh Fe@Pd/SiC, mainly resulting from the core−shell structure being partly changed into FePd alloy. Fe atoms with a lower Gibbs free energy continually migrate from the core to the surface of Fe@Pd nanoparticles in the course of the cyclic reaction. Meanwhile, the introduction of Fe may increase the surrounding electron cloud density around

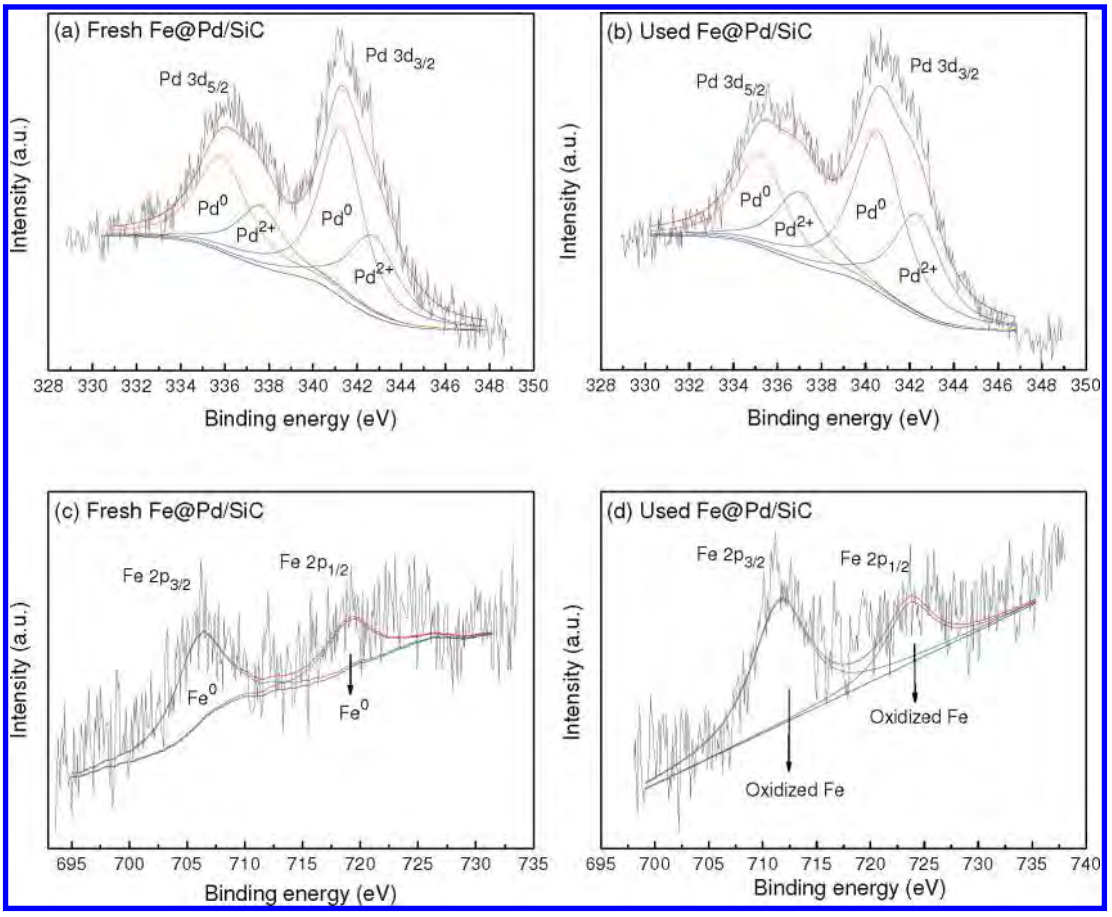

Figure 5. XPS spectra of Pd 3d (a, b) and Fe 2p (c, d) levels of fresh and used Fe@Pd/SiC.

Table 3. Binding Energies (eV) of Pd 3d, Pt 4f, Au 4f, and Fe 2p and the Surface Atomic Ratios of Different Fresh and Used Catalysts

	binding energy (eV)										
sample	Pd $3d_{5/2}$		Pd $3d_{3/2}$		Pt $4f_{7/2}$	Pt $4f_{5/2}$	Au $4f_{7/2}$	Au $4f_{5/2}$	Fe $2p_{3/2}$	Fe $2p_{1/2}$	atomic ratio Pd (Pt or Au)/Fe
fresh Fe@Pd/SiC	335.8	337.6	341.2	342.6					706.5	719.5	69:31
used Fe@Pd/SiC	335.4	337.0	340.7	342.3					711.3	723.9	51:49
fresh Fe@Pt/SiC					71.6	75.2			706.6	719.5	70:30
used Fe@Pt/SiC					71.1	74.8			711.4	723.8	46:54
fresh Fe@Au/SiC							84.1	87.8	706.6	719.7	73:27
used Fe@Au/SiC							84.0	87.9	711.3	724.0	71:29

Pd.[40,41] As a result, the corresponding peaks of Pd^0 and Pd^{2+} shift to lower binding energies. In addition, the main active phase of Pd-based catalysts for methane combustion is PdO, and the intensity of Pd−O bond determines the activity of catalyst.[19,20] The Pd−O bond can become weak when the electron cloud density around Pd atoms increases. Thus, the CH_4 dissociated species on active sites are more easily oxidized by dissociated O species. Moreover, the products are also more easily desorbed from the active sites. As a result, the activity of Fe@Pd/SiC increases with the cyclic times.

The Fe $2p_{3/2}$ and Fe $2p_{1/2}$ BE values at 706.6 and 719.5 eV are attributed to metallic Fe, whereas the Fe $2p_{3/2}$ and Fe $2p_{1/2}$ at 711.3 and 723.9 eV are indexed to Fe^{3+}.[42−44] Therefore, the Fe component in fresh and reacted Fe@Pd/SiC exists as Fe^0 and Fe^{3+}. However, the intensity of Fe 2p peaks of used Fe@Pd/SiC is larger than that of the fresh one mainly because a large quantity Fe atoms has migrated from cores to the surface of Fe@Pd nanoparticles. The surface atomic ratios shown in Table 3 further confirmed this result.

Figures 6 and 7 show the XPS spectra of fresh and used Fe@Pt/SiC and Fe@Au/SiC. The corresponding BE values are also listed in Table 3. The main Pt component of used Fe@Pt/SiC is Pt^0 because PtO and/or PtO_2 are easily decomposed into Pt at higher temperatures. The Pt BE values of used Fe@Pt/SiC are lower than those of the fresh one because the Fe@Pt core−shell structure has changed into FePt alloy. The main active phases in Pt-based catalysts for methane combustion are metallic Pt, which is different with Pd-based catalysts.[20] The increase

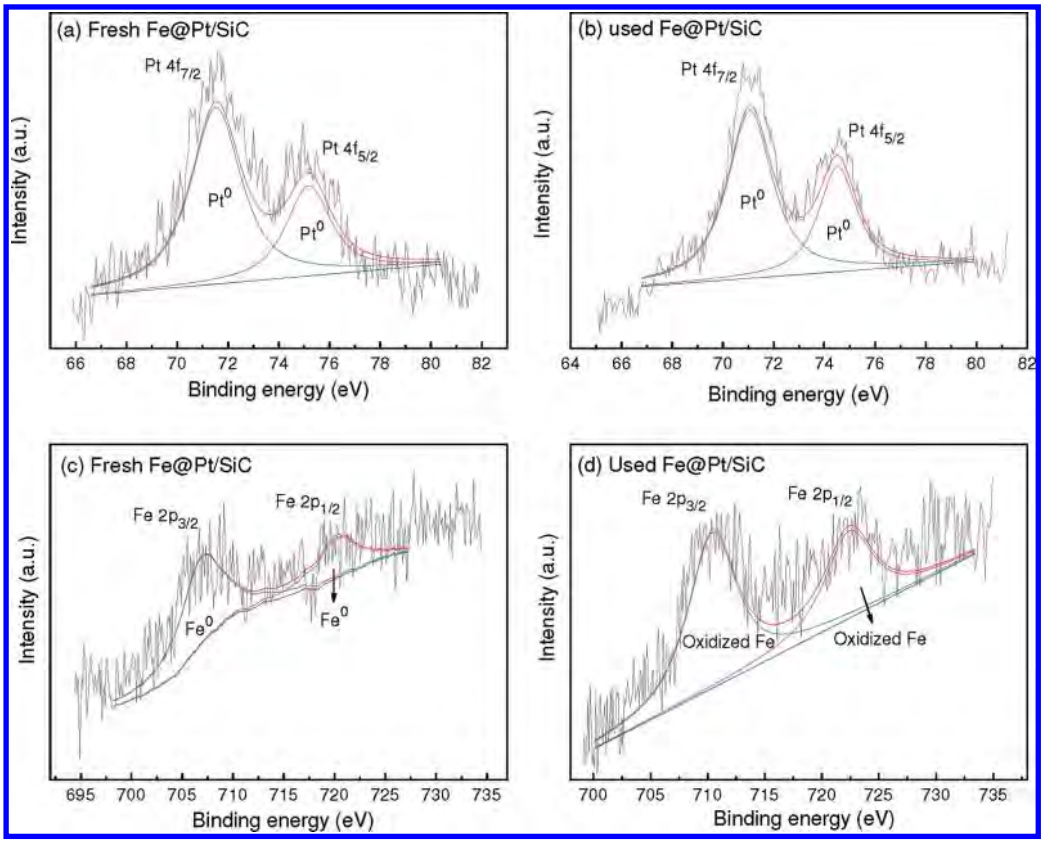

Figure 6. XPS spectra of Pt 4f (a, b) and Fe 2p (c, d) levels of fresh and used Fe@Pt/SiC.

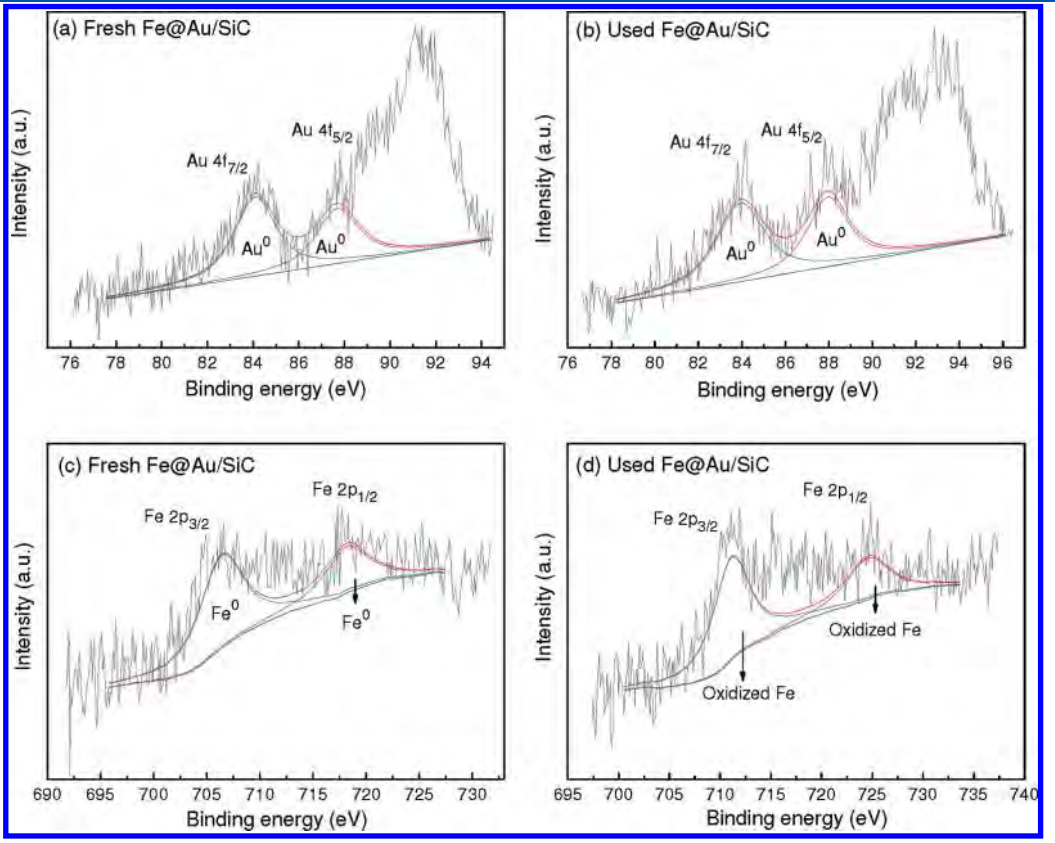

Figure 7. XPS spectra of Au 4f (a, b) and Fe 2p (c, d) levels of fresh and used Fe@Au/SiC.

dx.doi.org/10.1021/jp206606r |J. Phys. Chem. C 2011, 115, 24164–24171

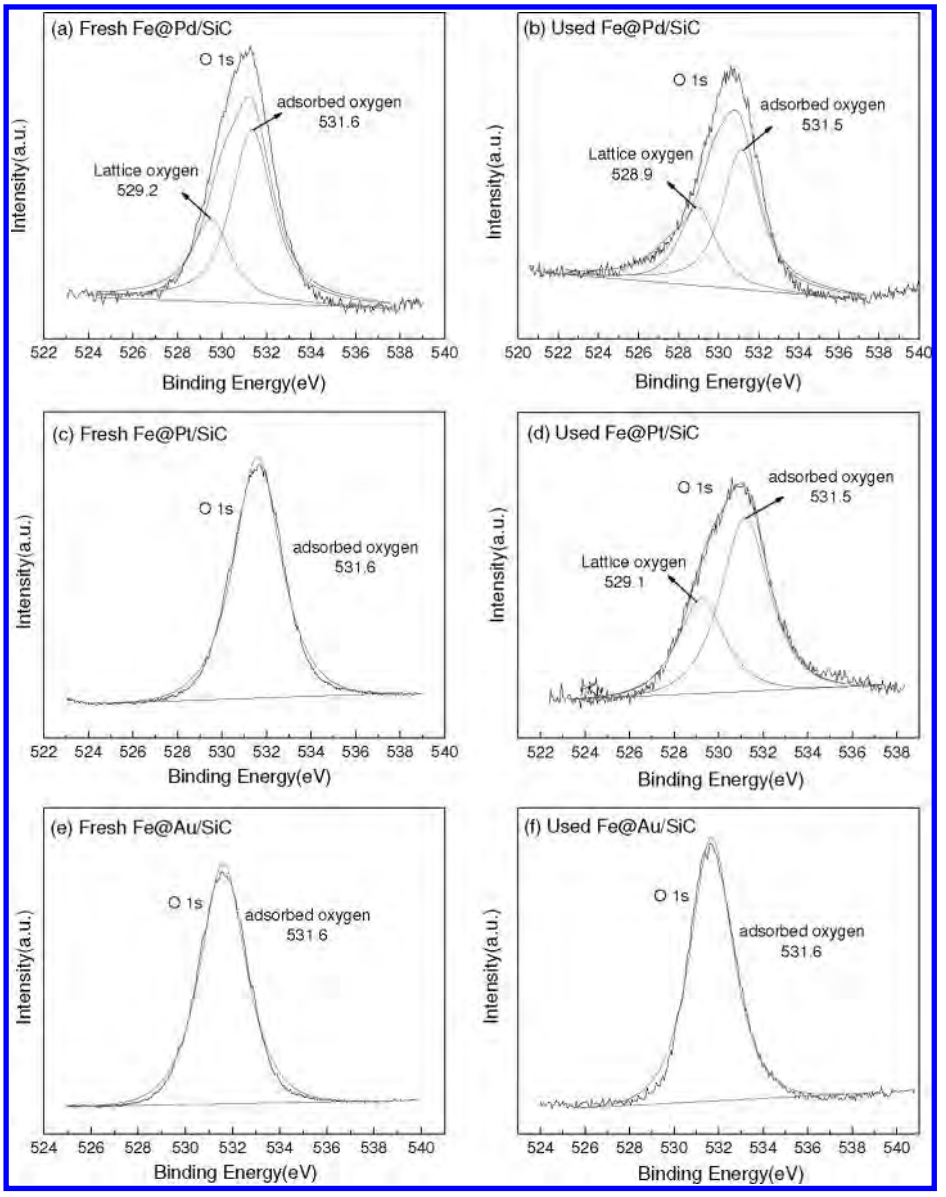

Figure 8. XPS spectra of O 1s levels of fresh and used Fe@Pd/SiC (a, b), Fe@Pt/SiC (c, d), and Fe@Au/SiC (e, f).

of surface Fe atoms significantly weakens the Pt−O bond.[45] Therefore, the gradually weakening of Pt−O bonds results in the increasing activity of Fe@Pt/SiC with the cyclic times. By comparing with Figure 6c,d, it is obvious that the intensities of Fe 2p peaks in used reacted Fe@Pt/SiC catalyst are also larger than those of the fresh one. No obvious changes can be seen from Figure 7, suggesting that the Fe@Au core−shell structure does not change during the reaction.

O 1s spectra of different catalysts are shown in Figure 8. The O 1s BE value at about 529.1 eV is attributed to the lattice oxygen associated with metal oxides, whereas the O 1s BE value at about 531.6 eV is attributed to absorbed oxygen.[46] Comparing Figure 8a,b, it can be seen that the BE values of O 1s in Fe@Pd/SiC slightly shift to lower binding energies after reaction. This further confirms that the increase of the surrounding electron cloud density around Pd can weaken the intensity of the Pd−O bond and then lower the BE values of lattice oxygen. From Figure 8c,e, only absorbed oxygen was detected in fresh Fe@Pt/SiC and Fe@Au/SiC, suggesting that the metal components in the two fresh catalysts are metallic phase. In Figure 8d, the lattice oxygen in used Fe@Pt/SiC can be attributed to Fe−O, while the BE value of adsorbed oxygen has a little decrease since the Pt−O bonds continually weaken during the reaction. No change of absorbed oxygen BE values in the Fe@Au/SiC has been found from Figure 8f, indicating that the Fe@Au core−shell nanoparticles are very stable in the methane catalytic combustion reaction.

4. CONCLUSION

Silicon carbide-supported Fe@Pd, Fe@Pt, and Fe@Au core−shell bimetallic catalysts were prepared by plasma sputtering deposition for methane catalytic combustion. All the core−shell catalysts exhibit higher activities than the corresponding single metallic catalysts due to the near surface alloying effects. With the structural evolution of Fe@Pd and Fe@Pt nanoparticles from

the core−shell structure to the alloy, the Pd−O and Pt−O bonds become weaker and weaker. As a result, the catalytic activities of Fe@Pd/SiC and Fe@Pt/SiC can increase gradually with the cyclic reaction times. XPS and HRTEM results further confirm that the surface Fe concentration of Fe@Pd/SiC and Fe@Pt/SiC continually increase and the core−shell structures gradually change into alloy structures during the reaction, whereas the activity of Fe@Au/SiC is very stable due to the stability of the Fe@Au core−shell structure in the reaction.

AUTHOR INFORMATION

Corresponding Author

*Fax: +33- 2 38 41 71 54 (P.B.), Fax/Tel: +86-351 4065282 (X.G.). Tel: +33- 2 38 41 71 25 (P.B.). E-mail: Pascal.Brault@univ-orleans.fr (P.B.), xyguo@sxicc.ac.cn (X.G.).

ACKNOWLEDGMENT

The work was financially supported by NSFC (ref. 20973190), the in-house research project of SKLCC (ref. SKLCC-2008BWZ010), and the National Basic Research Program (ref. 2011CB201405).

REFERENCES

(1) Enache, D. I.; Edwards, J. K.; Landon, P.; Solsona-Espriu, B.; Carley, A. F.; Herzing, A. A.; Watanabe, M.; Kiely, C. J.; Knight, D. W.; Hutchings, G. J. *Science* **2006**, *311*, 362–365.

(2) Edwards, J. K.; Solsona, B. E.; Landon, P.; Carley, A. F.; Herzing, A. A.; Kiely, C. J.; Hutchings, G. J. *J. Catal.* **2005**, *236*, 69–79.

(3) Edwards, J. K.; Thomas, A.; Carley, A. F.; Herzing, A. A.; Kiely, C. J.; Hutchings, G. J. *Green Chem.* **2008**, *10*, 388–394.

(4) Yang, H. *Angew. Chem., Int. Ed.* **2011**, *50*, 2674–2676.

(5) Peng, Z. M.; Yang, H. *Nano Today* **2009**, *4*, 143–164.

(6) Hsieh, Y. C.; Chang, L. C.; Wu, P. W.; Chang, Y. M.; Lee, J. F. *Appl. Catal., B* **2011**, *103*, 116–127.

(7) Silva, J. C. M.; De Souza, R. F. B.; Parreira, L. S.; Teixeira Neto, E.; Calegaro, M. L.; Santos, M. C. *Appl. Catal., B* **2010**, *99*, 265–271.

(8) Tao, F.; Grass, M. E.; Zhang, Y. W.; Butcher, D. R.; Renzas, J. R.; Liu, Z.; Chung, J. Y.; Mun, B. S.; Salmeron, M.; Somorjai, G. A. *Science* **2008**, *322*, 932–934.

(9) Mizukoshi, Y.; Sato, K.; Konno, T. J.; Masahashi, N. *Appl. Catal., B* **2010**, *94*, 248–253.

(10) Dabbousi, B. O.; Rodriguez-Viejo, J.; Mikulec, F. V.; Heine, J. R.; Mattoussi, H.; Ober, R.; Jensen, K. F.; Bawendi, M. G. *J. Phys. Chem. B* **1997**, *101*, 9463–9475.

(11) Pastoriza-Santos, I.; Koktysh, D. S.; Mamedov, A. A.; Giersig, M.; Kotov, N. A.; Liz-Marzan, L. M. *Langmuir* **2000**, *16*, 2731–2735.

(12) Teng, X. W.; Black, D.; Watkins, N. J.; Gao, Y. L.; Yang, H. *Nano Lett.* **2003**, *3*, 261–264.

(13) Liu, X. G.; Geng, D. Y.; Meng, H.; Cui, W. B.; Yang, F.; Kang, D. J.; Zhang, Z. D. *Solid State Commun.* **2009**, *149*, 64–67.

(14) Rabat, H.; Andreazza, C.; Brault, P.; Caillard, A.; Béguin, F.; Charles, C.; Boswell, R. *Carbon* **2009**, *47*, 209–214.

(15) Berthet, A.; Thomann, A. L.; Cadete Santos Aires, F. J.; Brun, M.; Deranlot, C.; Bertolini, J. C.; Rozenbaum, J. P.; Brault, P.; Andreazzaz, P. *J. Catal.* **2000**, *190*, 49–59.

(16) Zhang, H. X.; Wang, C.; Wang, J. Y.; Zhai, J. J.; Cai, W. B. *J. Phys. Chem. C* **2010**, *114*, 6446–6451.

(17) Ito, Y.; Miyazaki, A.; Valiyaveettil, S.; Enoki, T. *J. Phys. Chem. C* **2010**, *114*, 11699–11702.

(18) Guo, X. N.; Brault, P.; Zhi, G. J.; Caillard, A.; Jin, G. Q.; Coutanceau, C.; Baranton, S.; Guo, X. Y. *J. Phys. Chem. C* **2011**, *115*, 11240–11246.

(19) Ciuparu, D.; Lyubovsky, M. R.; Altman, E.; Pfefferle, L. D.; Datye, A. *Catal. Rev.* **2002**, *44*, 593–649.

(20) Gélin, P.; Primet, M. *Appl. Catal., B* **2002**, *39*, 1–37.

(21) Zwinkels, M. F. M.; Järås, S. G.; Menon, P. G.; Griffin, T. A. *Catal. Rev.* **1993**, *35*, 319–358.

(22) Choudhary, V. R.; Patil, V. P.; Jana, P.; Uphade, B. S. *Appl. Catal., A* **2008**, *350*, 186–190.

(23) Rabat, H.; Brault, P. *Fuel Cells* **2008**, *8*, 81–86.

(24) Thomann, A. L.; Brault, P.; Rozenbaum, J. P.; Andreazza-Vignolle, C.; Andreazza, P.; Estrade-Szwarckopf, H.; Rousseau, B.; Babonneau, D.; Blondiaux, G. *J. Phys. D: Appl. Phys.* **1997**, *30*, 3197–3202.

(25) Jin, G. Q.; Guo, X. Y. *Microporous Mesoporous Mater.* **2003**, *60*, 207–212.

(26) Guo, X. Y.; Jin, G. Q. *J. Mater. Sci.* **2005**, *40*, 1301–1303.

(27) Guo, X. N.; Shang, R. J.; Wang, D. H.; Jin, G. Q.; Guo, X. Y.; Tu, K. N. *Nanoscale Res. Lett.* **2010**, *5*, 332–337.

(28) Guo, X. N.; Zhi, G. J.; Yan, X. Y.; Jin, G. Q.; Guo, X. Y.; Brault, P. *Catal. Commun.* **2011**, *12*, 870–874.

(29) Farrauto, R. J.; Hobson, M. C.; Kennelly, T.; Waterman, E. M. *Appl. Catal., A* **1992**, *81*, 227–237.

(30) Ozawa, Y.; Tochihara, Y.; Nagai, M.; Omi, S. *Chem. Eng. Sci.* **2003**, *58*, 671–677.

(31) Wang, G. X.; Wu, H. M.; Wexler, D.; Liu, H. k.; Savadogo, O. *J. Alloys Compd.* **2010**, *503*, L1–L4.

(32) Sato, K.; Kovács, A.; Hirotsu, Y. *Thin Solid Films* **2011**, *519*, 3305–3311.

(33) Dai, H. J.; Rinzler, A. G.; Nikolaev, P.; Thess, A.; Colbert, D. T.; Smalley, R. E. *Chem. Phys. Lett.* **1996**, *260*, 471–475.

(34) Jiang, Q.; Lu, H. M. *Surf. Sci. Rep.* **2008**, *63*, 427–464.

(35) Zeng, H.; Li, J.; Wang, Z. L.; Liu, J. P.; Sun, S. H. *Nano Lett.* **2004**, *4*, 187–190.

(36) Nelson, A. E.; Schulz, K. H. *Appl. Surf. Sci.* **2003**, *210*, 206–221.

(37) Arai, H.; Machida, M. *Catal. Today* **1991**, *10*, 81–94.

(38) Gao, Z. H.; Liu, Z. C.; He, F.; Xu, G. H. *J. Mol. Catal. A* **2005**, *235*, 143–149.

(39) Babu, N. S.; Lingaiah, N.; Kumar, J. V.; Prasad, P. S. S. *Appl. Catal., A* **2009**, *367*, 70–76.

(40) Lambrou, P. S.; Efstathiou, A. M. *J. Catal.* **2006**, *240*, 182–193.

(41) Lambrou, P. S.; Savv, P. G.; Fierro, J. L. G.; Efstathiou, A. M. *Appl. Catal., B* **2007**, *76*, 375–385.

(42) Zhang, X. B.; Yan, J. M.; Han, S.; Shioyama, H.; Xu, Q. *J. Am. Chem. Soc.* **2009**, *131*, 2778–2779.

(43) Bi, Y. S.; Chen, L.; Lu, G. X. *J. Mol. Catal. A* **2007**, *266*, 173–179.

(44) Bajnóczi, É. G.; Balázs, N.; Mogyorósi, K.; Srankó, D. F.; Pap, Z.; Ambrus, Z.; Canton, S. E.; Norén, K.; Kuzmann, E.; Vértes, A.; Homonnay, Z.; Oszkó, A.; Pálinkó, I.; Sipos, P. *Appl. Catal., B* **2011**, *103*, 232–239.

(45) Mahata, N.; Gonçalves, F.; Pereira, M. F. R.; Figueiredo, J. L. *Appl. Catal., A* **2008**, *339*, 159–168.

(46) Wang, S. P.; Zheng, X. C.; Wang, X. Y.; Wang, S. R.; Zhang, S. M.; Yu, L. H.; Huang, W. P.; Wu, S. H. *Catal. Lett.* **2005**, *105*, 163–168.